



INVERSE INTEGRATION METHOD FOR DISTRIBUTED SOUND SOURCES

Roberto Merino-Martínez¹, Pieter Sijtsma^{1,2} and Mirjam Snellen¹

¹Aircraft Noise & Climate Effects section, Faculty of Aerospace Engineering, Delft University of Technology
Kluyverweg 1, 2629 HS Delft, The Netherlands

²Pieter Sijtsma Advanced AeroAcoustics (PSA3)
Prinses Margrietlaan 13, 8091 AV Wezep, The Netherlands

Abstract

Most acoustic imaging methods assume the presence of point sound sources and, hence, fail to correctly estimate the sound emissions of distributed sound sources (such as trailing-edge noise). In this contribution, three integration techniques are suggested to overcome this issue based on models considering a single point source, a line source and several line sources, respectively. Two simulated benchmark cases featuring distributed sound sources are used to compare the performance of these integration techniques with respect to other well-known methods. The considered integration methods provide the best performance in retrieving the source levels and require short computational times. In addition, the presence of unwanted noise sources, such as corner sources in wind-tunnel measurements, no longer affects the results negatively when using the last method. A sensitivity analysis shows that the integration technique based on a line source is robust with respect to the choice of the integration area (shape, position and mesh fineness). Practical recommendations are provided for the application of these methods to experimental cases.

1 INTRODUCTION

Conventional acoustic beamforming techniques [1–3] normally assume the presence of point sound sources. In practice, however, noise sources are often distributed over extended regions, like along the edges of aircraft wings [4–8] or wind turbine blades [4, 9–17]. As a result, conventional methods do not yield the correct emitted noise levels. To overcome this issue, the Source Power Integration (SPI) technique [10, 18] was proposed, which basically sums and scales the results of conventional frequency domain beamforming (CFDBF) over (part of) a

scan grid. The idea is to, in this way, retrieve the source level of a distributed source, i.e., a single value.

A drawback of the SPI technique is that the results can be contaminated by the response of noise sources outside the region of integration (ROI). For example, airfoil trailing-edge noise sources measured in wind-tunnel experiments can be heavily contaminated by “corner” sources appearing at the junctions of the airfoil and the wind-tunnel walls or end plates.

To obtain better results in the above-sketched circumstances, extensions of the SPI method can be considered:

- An extension of the SPI assuming the presence of a line source instead of a monopole source (SPIL) can easily be derived [19]. This technique was applied previously to synthetic data of trailing-edge noise in a closed-section wind-tunnel measurement heavily contaminated by background noise, within the Phased-Array Methods Benchmark [20–23], see section 3.1. The task was to calculate the sound spectrum emitted by the line source. The SPIL method presented the best results for this case [19], compared to other well-known methods, such as CLEAN-SC [24–26], DAMAS [27], functional beamforming [28–31], Covariance Matrix Fitting (CMF) [32] or orthogonal beamforming [33–35].
- A generalization of the SPIL technique to distributed sound sources on multiple ROIs, called Inverse SPI (ISPI), is introduced in this paper and applied to realistic wind-tunnel simulations of trailing-edge noise contaminated by corner sources.

This paper is structured as follows: Section 2 briefly explains the basics of the SPI, SPIL and ISPI techniques. The simulation setups employed for the evaluation of these methods are introduced in section 3. Section 4 presents the comparison between the results obtained by the aforementioned integration methods, as well as other well-known acoustic imaging methods. Section 5 contains a detailed sensitivity analysis of the SPIL technique with respect to some practical parameters, such as the size and shape of the ROI. Finally, section 6 gathers the main conclusions.

2 METHOD EXPLANATION

For well-separated monopole sources, CFDBF provides the correct source sound pressure levels L_p as the peak levels in the source map [36]. This situation, however, rarely occurs in practice, where the main lobes of different sound sources can overlap, sidelobes deteriorate the source map, and the sound source can be spatially distributed, such as for trailing edge noise. In these cases, the peak levels obtained from CFDBF correspond to erroneous source levels. In addition, if coherence loss [37] applies, the main lobe becomes broader and gets reduced in strength [36].

To mitigate all these issues, different integration methods have been proposed. Three of them are described below, in increasing order of sophistication.

2.1 Source Power Integration (SPI)

The Source Power Integration (SPI) technique [10, 18] was proposed in order to limit the influence of the array point spread function (PSF). This technique sums the source autopowers

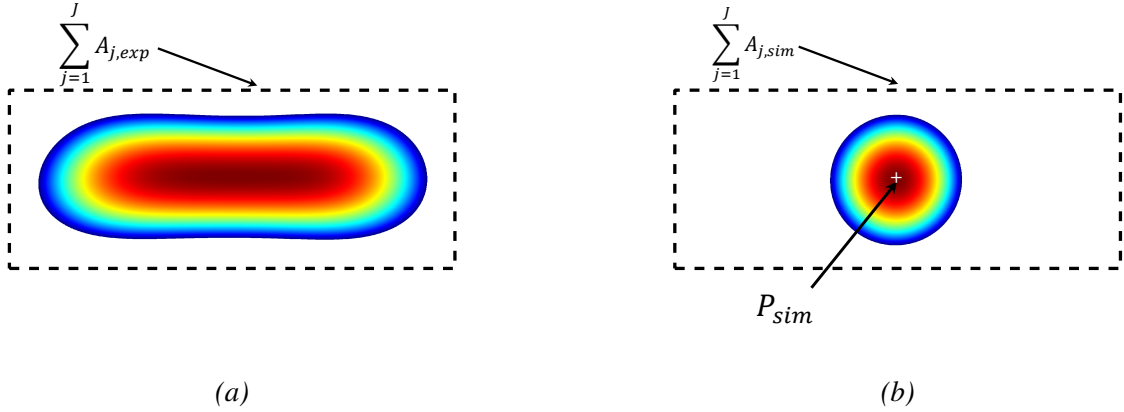


Figure 1: (a) Example of the application of the SPI technique: Experimental distributed sound source and (b) simulated point source. The dashed black rectangle denotes the ROI, and the white + marker the location of the simulated point source.

A_j in a ROI of the source map selected by the user containing J grid points and corrects the result with a scaling factor obtained by performing a simulation for a monopole source located within the ROI at grid point ξ_k , with steering vector \mathbf{g}_k [10] (typically situated at the center of the ROI), see Fig. 1b. The integrated source power P_{exp} per frequency on the ROI is calculated as:

$$P_{exp} = \sum_{j=1}^J A_{j,exp} \frac{P_{sim}}{\sum_{j=1}^J A_{j,sim}} = \sum_{j=1}^J (\mathbf{w}_j^* \mathbf{C} \mathbf{w}_j) \frac{P_{sim}}{\sum_{j=1}^J (\mathbf{w}_j^* (\mathbf{g}_k \mathbf{g}_k^*) \mathbf{w}_j)}, \quad (1)$$

where P_{sim} is the sound power of the simulated source (normally taken as unity), J is the number of grid points in the ROI, \mathbf{C} is the cross-spectral matrix (CSM) [10], and $A_{j,exp}$ and $A_{j,sim}$ are the experimental and simulated beamforming results, respectively [36]. The term \mathbf{w}_j refers to the weighted steering vector defined as $\mathbf{w}_j = \mathbf{g}_j / \|\mathbf{g}_j\|^2$ [10].

If the main diagonal of CSM is removed, the negative source power estimates need to be neglected in the summations in Eq. (1) because they have no physical meaning [10]. Another option is to exclude all the source power estimates under a threshold value (such as 12 dB) below the peak level in the source map [10].

The ROI should include the complete sound source (see Fig. 1a) to be analyzed and be large enough to capture the potential main-lobe broadening due to coherence loss [36]. However, the variation of the array resolution should be small within the ROI and the choice of the ROI should also avoid the contributions and sidelobes from other sound sources and the noise floor from the source map [36].

This integration technique has been successfully applied to several wind-tunnel experiments [4, 9–14, 19] and aircraft flyover measurements [8, 38, 39], yielding accurate sound pressure levels, even in the cases when coherence loss is present [36]. A similar integration technique can be applied to the results obtained with functional beamforming [39].

2.2 Extension to line sources (SPIL)

If the shape of the distributed sound source resembles a line, such as for the leading- or trailing-edge noise of an airfoil, a simulated line source can be considered for normalization, instead of a point source as done in the SPI technique, to model the physics of the experiment in a better way. In practice, a large number K of simulated incoherent point sources of equal power level are placed along the expected location of the experimental line source with steering vectors $\mathbf{g}_k, k \in [1 \dots K]$. A minimization problem for the difference between the measured CSM (\mathbf{C}) and the CSM corresponding to the line source, \mathbf{L} , is then formulated:

$$\min \|\mathbf{C} - P_{\text{exp}} \mathbf{L}\|^2, \quad (2)$$

where \mathbf{L} is the CSM due to the simulated line source of unit strength. By solving Eq. (2) for P_{exp} using a least-squares approach, Eq. (1) is updated as:

$$P_{\text{exp}} = \frac{\sum_{j=1}^J (\mathbf{g}_j^* \mathbf{C} \mathbf{g}_j) P_{\text{sim}}}{\sum_{j=1}^J (\mathbf{g}_j^* (\sum_{k=1}^K \mathbf{g}_k \mathbf{g}_k^*) \mathbf{g}_j)}. \quad (3)$$

where P_{sim} here is due to all the K simulated sources.

For distributed sound sources, the source coherence should be taken into account. However, the coherence length of a source is typically much smaller than the main lobe width, so the assumption of distributed incoherent monopoles is, in essence, valid [36].

This technique has already been applied to trailing-edge noise measurements in an open-jet [13] and a closed-section wind tunnel [15].

2.3 Inverse SPI (ISPI)

In case the SPI method is extended even more by considering multiple ROIs in which the source powers of the simulated sources differ for the different ROIs, a more general method called Inverse SPI (ISPI) is obtained. Thus, a similar minimization problem as the one presented in Eq. (2) considering Z different ROIs simultaneously (each of them with different sound powers $P_{\text{exp},z}$) can be formulated:

$$\min \left\| \mathbf{C} - \sum_{z=1}^Z P_{\text{exp},z} \mathbf{L}_z \right\|^2, \quad (4)$$

The Z ROIs can have different sizes. This problem needs to be solved under the non-negativity constraints of $P_{\text{exp},z} \geq 0$. A standard Non-Negative Least Squares (NNLS) solver can be used [40].

This integration technique is especially useful for wind-tunnel measurements featuring mounting plates for the test model, which can cause extraneous noise sources on the junction between the test model and the mounting plates, also known as ‘‘corner’’ sources [41]. These sources can contaminate the results of the ROI of interest in experiments [11–14, 42], so the ISPI technique can exclude their influence in the actual results.

If this method is taken to the limit of considering each single grid point as a ROI (i.e., $Z = J$), the obtained method is, in essence, DAMAS [27].

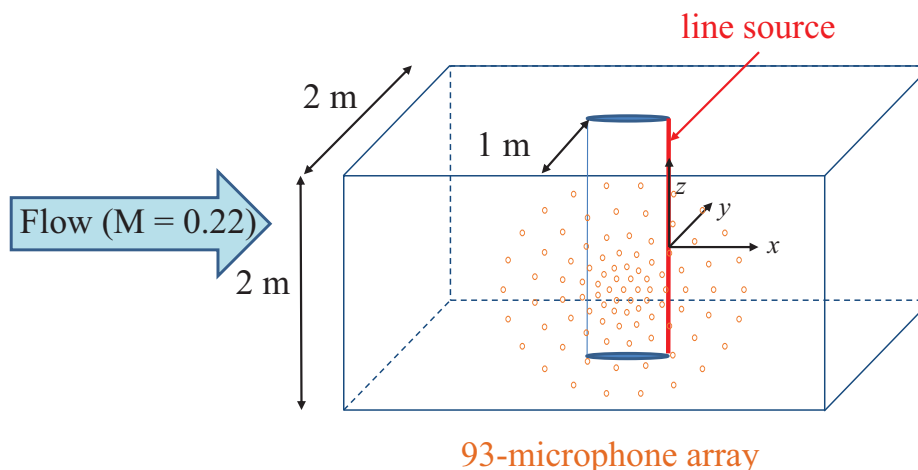


Figure 2: Diagram explaining the computational setup for the line source benchmark case. Adapted from [19].

3 DESCRIPTION OF THE SYNTHETIC TEST CASES

3.1 Line-source benchmark

This benchmark case is part of the Phased-Array Methods Benchmark¹ [20–23] and consists of microphone-array measurements of a simulated line source severely affected by incoherent noise. It represents a typical measurement of trailing-edge noise in a closed-section wind tunnel with microphones flush-mounted in a wall of the tunnel, where the signals recorded by the microphones also include the noise of the wall-boundary-layer turbulence [19].

This benchmark case was proposed by Pieter Sijtsma (PSA3) [43] and the preliminary results obtained by several researchers using different acoustic imaging methods have been published recently by Sarradj et al. [19].

The considered coordinate system is shown in Fig. 2, with the x axis in the flow direction, the y axis perpendicular to the line source and pointing away from the array plane, the z axis in the spanwise direction of the line source pointing upwards and the center in the middle of the line source.

A 2-m-long line source with short correlation length was simulated between $z = -1$ m and $z = 1$ m located at $x = y = 0$, inside of a $2\text{ m} \times 2\text{ m}$ cross section of a wind tunnel, see Fig. 2. Henceforth, this line source is referred to as “experimental” line source, see Fig. 3. A uniform flow with a Mach number of $M = 0.22$ was modeled in the x -direction. A 93-microphone array distributed in concentric circles and located at the $y = -1$ m plane with a diameter of 1.8 m was considered, see Fig. 2. The presence of hard wind-tunnel walls was neglected for the simulations, i.e., no reflections are present.

A detailed explanation of the signal generation process can be found in [19]. The line source

¹The acoustic data and more details of this benchmark case (B1) are currently available online in the following website: <https://www-fs.tu-cottbus.de/aeroakustik/analytical/>.

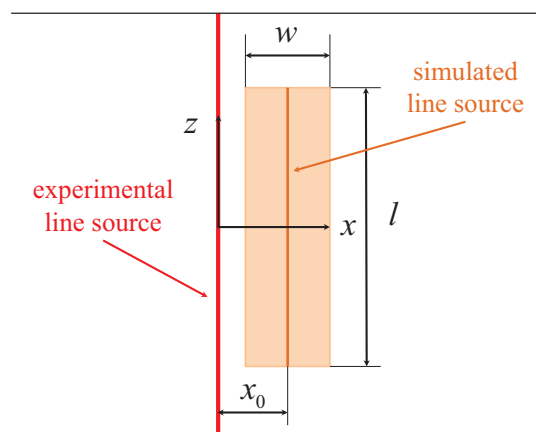


Figure 3: Diagram explaining the parameters that define the ROI (shaded in orange).

was simulated as a large number of incoherent monopoles at equal spacing and equal strengths. This results in a source strength distribution per unit length denoted as \tilde{A} in Pa^2/m . The exact solution per frequency f for this benchmark case expressed as the sound pressure level (L_p) at the center microphone of the array, $(x, y, z) = (0, -1, 0)$ m, in dB and 50 Hz steps (resulting in a total of 200 frequencies from 50 Hz to 10 kHz) was selected to be:

$$L_p = 61.16 + 0.34127 \frac{f}{1000} + 0.87242 \left(\frac{f}{1000} \right)^2 - 0.163 \left(\frac{f}{1000} \right)^3 + 0.0082341 \left(\frac{f}{1000} \right)^4. \quad (5)$$

On top of the signal generated by the line source, Gaussian white noise incoherent from microphone to microphone was added with an L_p of 86.89 dB per frequency considered. This provides negative signal to noise ratio (SNR) values for the whole frequency range (between -25.7 dB at 50 Hz to -15.7 dB at 10 kHz), due to the varying source strength with frequency.

The challenge of this benchmark is to obtain the value of \tilde{A} per frequency, expressed as the L_p at the center of the array $(x, y, z) = (0, -1, 0)$ m using the following expression [19, 43]

$$L_p = 10 \log_{10} \left\{ \frac{\tilde{A}}{8\pi^2(1-M^2)p_{e,0}^2 h} \left[\arctan \left(\frac{l}{2h} \right) \right] \right\}, \quad (6)$$

where h represents the distance between the array plane and the scan plane, l is the length of the ROI in the spanwise direction (symmetric with respect to the $z = 0$ plane), see Fig. 3, and $p_{e,0}$ is the reference effective pressure of $20 \mu\text{Pa}$. This way of expressing the results was selected in order to compare the results of different contributions to the benchmark, and represents the L_p experienced at that position if only the line source would be present.

For this case, $h = 1$ m and $l = 2$ m, so Eq. (6) can be simplified to

$$L_p = 10 \log_{10} \left(\frac{\tilde{A}}{32\pi(1-M^2)p_{e,0}^2} \right). \quad (7)$$

3.2 Line–source and corner sources

To investigate the merits of ISPI, an additional array simulation was considered. The same microphone array was used as in section 3.1. A line source was simulated at the same position, and also the same Mach number was used. The source strength distribution \tilde{A} was selected such that the induced L_p (via Eq. (6)) in the central microphone of the array was exactly 80 dB. In addition, two incoherent point sources were placed at both ends of the line, representing “corner sources” due to interaction of the airfoil with the boundary layers of the wind–tunnel walls. These two corner sources led to an increase in L_p of more than 3 dB at the central microphone. In this simulation, no incoherent noise was added.

The challenge is to obtain \tilde{A} , while minimizing the influence of the corner sources.

4 RESULTS DISCUSSION

4.1 Line–source benchmark

A preliminary study of the acoustic data using CFDBF confirmed that removing the main diagonal of the CSM [10] is necessary since the SNR values are very low and the influence of incoherent noise is very strong. The convection of the sound waves due to the movement of the flow inside the wind tunnel also needs to be taken into account for obtaining valid results [10]. Four source plot examples for the whole frequency range (50 Hz to 10 kHz) are presented in Fig. 4 to illustrate this phenomena. The overall sound pressure levels ($L_{p,\text{overall}}$) are presented. This metric in a spectrum with K frequencies is defined as

$$L_{p,\text{overall}} = 10 \log_{10} \left(\sum_{k=1}^K 10^{L_{p,k}/10} \right). \quad (8)$$

Figure 4a shows the beamforming results without applying the diagonal removal (DR) or convective effects; Figure 4b includes convective effects but no DR; Figure 4c includes DR but no convective effects and Figure 4d includes both effects. In Figs. 4a and 4b, the incoherent noise hinders any useful interpretation of the source plot and the presence of the line can barely be detected. Moreover, the $L_{p,\text{overall}}$ values in these figures are considerably higher than they should be. After applying DR (see Fig. 4c) the line source is clearly visible, and located at the correct position if the convective effects are accounted for (see Fig. 4d).

Several well–known acoustic imaging methods (orthogonal beamforming, CMF, functional beamforming, SPI, SPIL, DAMAS and CLEAN–SC) were applied by different researchers using the parameters specified in Table 1. The solutions obtained with them were extracted from Sarradj et al. [19]. Only one solution per method is considered, but considerable differences were found when different contributors applied the same method, such as DAMAS or CLEAN–SC [19].

In the second column of Table 1, BTU corresponds to the Brandenburg University of Technology Cottbus – Senftenberg and TU Berlin in Germany, NASA to the NASA Langley Research Center in the United States, PSA3 to Pieter Sijtsma Advanced AeroAcoustics in the Netherlands, TU Delft to Delft University of Technology in the Netherlands, and UniA to the University of Adelaide in Australia [19]. In the third column of Table 1, the relevant parameters of each method are specified: DR stands for the removal of the main diagonal of the CSM, \hat{k} is

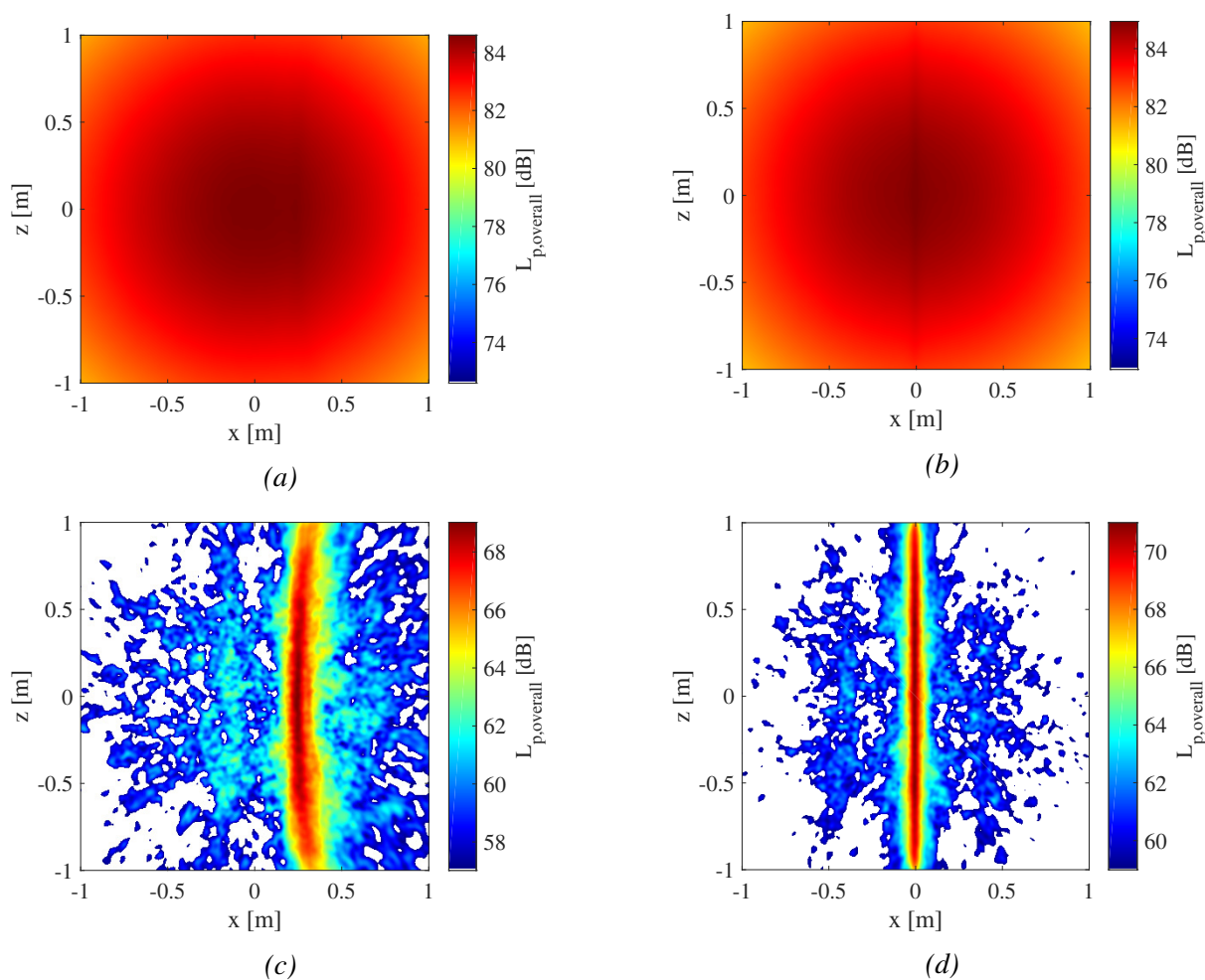


Figure 4: Obtained source maps with CFDBF for the whole frequency range (50 Hz to 10 kHz): (a) Without DR or considering convective effects. (b) Without DR of the CSM, but considering convective effects. (c) DR without considering convective effects. (d) DR and considering convective effects.

the number of eigenvalues considered for orthogonal beamforming, NNLS stands for the non-negative least squares method [44, 45], ν is the functional beamforming exponent, N_{iter} is the number of iterations for DAMAS, and $\tilde{\varphi}$ is the damping factor or loop gain for CLEAN-SC. The ROI employed by each contributor is stated in the fourth column of Table 1 in terms of width (w) \times length (l), see Fig. 3. The spacing between grid points Δx is included in the last column. All the contributors used ROIs centered at $x = 0$ and from $y = -1$ m to $y = 1$ m, i.e., the whole span.

The frequency spectra obtained by these methods for the line-source benchmark are presented in Fig. 5a. The relative errors of each method with respect to the exact solution, $\Delta L_p = L_p - L_{p,exact}$, are included in Fig. 5b. This way, a positive value of ΔL_p means that the method overpredicts the solution and vice versa. Moreover, the absolute errors made by each method averaged over the whole frequency range (i.e., over the 200 frequencies) $\varepsilon = |\overline{\Delta L_p}|$

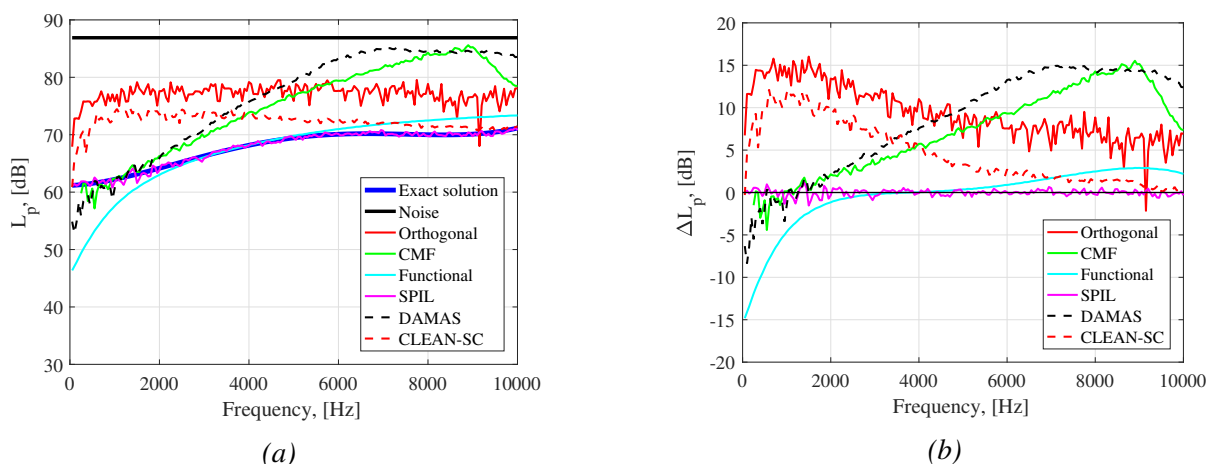


Figure 5: (a) Results of the line-source benchmark for different acoustic imaging methods. Adapted from [19]. (b) Relative errors ΔL_p with respect to the exact solution for each method.

are indicated in Table 2. In general, most methods tend to overpredict the spectrum (with the exception of functional beamforming below 2000 Hz). Orthogonal beamforming seems to considerably overpredict the results, especially at low frequencies, with errors up to about 15 dB. CMF and DAMAS present a similar behavior, but with increasing errors (up to 15 dB) for high frequencies. CLEAN-SC shows a similar trend as orthogonal beamforming but with errors about 5 dB lower. Functional beamforming seems to underpredict the results at low frequencies (below 2000 Hz), but provides acceptable results for higher frequencies. This might be a “lucky shot” since the main diagonal of the CSM was not removed [19]. Optimizing the diagonal of the CSM [46, 47], instead of removing it, is of interest for future research. SPIL (with a ROI width of $w = 0.04$ m) provides the best results for this case in the whole spectrum, with an average error lower than 0.3 dB and maximum errors of 1.2 dB. In addition, the computational time required by the SPIL method is considerably lower than other methods, especially DAMAS.

Table 1: Overview of the contributors and parameters for each method. Adapted from [19].

Method	Contributor	Parameters	ROI	Grid spacing (Δx)
Orthogonal	BTU	DR, $\hat{k} = 16$	0.2 m \times 2 m	0.025 m
CMF	BTU	DR, NNLS solver	0.2 m \times 2 m	0.025 m
SPI	PSA3 and UniA	DR	0.08 m \times 2 m	0.02 m
SPIL	TU Delft	DR	0.08 m \times 2 m	0.02 m
SPIL	TU Delft	DR	0.04 m \times 2 m	0.01 m
Functional	TU Delft	no DR, $\nu = 16$	0.1 m \times 2 m	0.01 m
DAMAS	NASA	DR, $N_{\text{iter}} = 200$	0.12 m \times 2 m	0.02 m
CLEAN-SC	UniA	DR, $\tilde{\varphi} = 0.99$	0.08 m \times 2 m	0.02 m

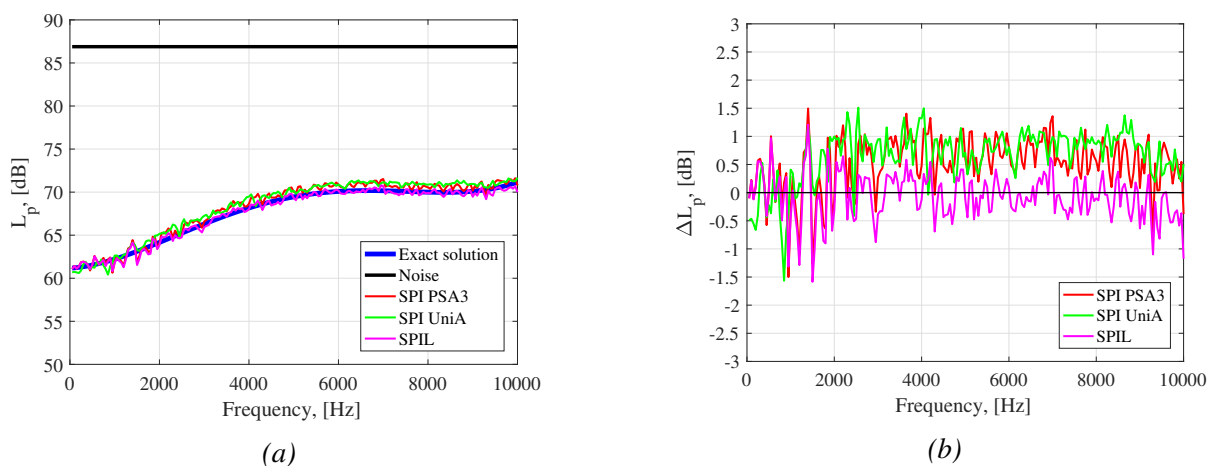


Figure 6: (a) Results of the line–source benchmark for the SPI and SPIL methods with $w = 0.08$ m. (b) Relative errors ΔL_p with respect to the exact solution for each method.

For clarity reasons, the solutions obtained by UniA and PSA3 using the SPI method were not included in Fig. 5 but instead, a separate study is presented in Fig. 6 comparing the performance of SPI and SPIL. In order to have a fair comparison all the ROI parameters were kept constant: $w = 0.08$ m, $l = 2$ m, $x_0 = 0$ and $\Delta x = 0.02$ m. Figure 6a presents the absolute spectra of both SPI and the SPIL contributions. It can be observed that the results collapse almost perfectly with the exact solution. The relative errors made by each method are depicted in Fig. 6b, with a considerably smaller scale in the y axis than in Fig. 5b. The three contributions provide similar results, with maximum errors for single frequencies of ± 1.5 dB. However, the average absolute error made by the SPI method ($\varepsilon \approx 0.65$ dB) is approximately double than the one made by the SPIL technique ($\varepsilon \approx 0.33$ dB), see Table 2. Therefore, the use of the SPIL method is recommended for this type of experiments, since it approximates the physics of the sound source in a better way.

The ISPI technique was not used in this benchmark case because all the incoherent monopoles had the same strength, and in this situation the ISPI technique is essentially the same as the SPIL method. A separate benchmark case to test the ISPI method is presented in section 4.2.

4.2 Line–source and corner sources

Typical acoustic images, obtained with CFDBF, of the line source simulation with corner sources are shown in Fig. 7 for different one–third–octave frequency bands. Beamforming was performed after DR and correcting for the convection effects. These images show that, at low frequencies, the line source tends to be completely masked by the corner sources.

An often used workaround for dealing with corner sources is to perform SPI on a reduced integration area in the middle of the span, away from the corners [42]. Due to the fact that L_p explicitly depends on the length of the ROI l , see Eq. (6), a correction factor needs to be applied to the obtained solutions. If the whole length of the experimental line source is selected for normalizing the results (i.e., $l = 2$ m), the L_p obtained with the reduced integration area of length l ($L_{p,l}$) can be corrected to full span by

Table 2: Average absolute errors made by each method with respect to the exact solution.

Method	ϵ , [dB]
Orthogonal ($k = 16$)	9.4034
CMF	7.2963
SPI PSA3 ($w = 0.08$ m)	0.6314
SPI UniA ($w = 0.08$ m)	0.7414
SPIL ($w = 0.08$ m)	0.3281
SPIL ($w = 0.04$ m)	0.2881
Functional ($v = 50$)	2.1741
DAMAS ($N_{\text{iter}} = 200$)	9.0901
CLEAN-SC	4.5769

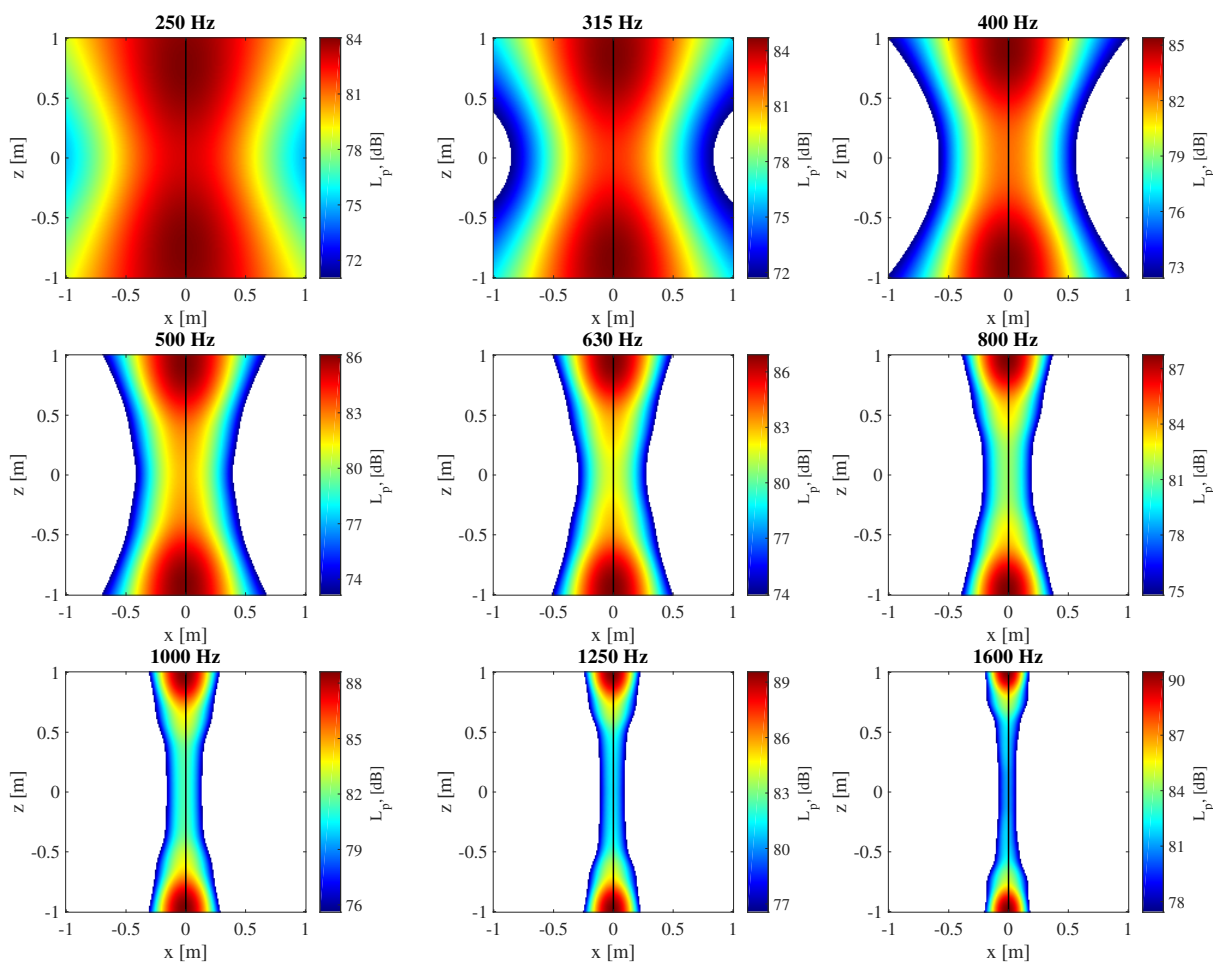


Figure 7: Source maps of the line source with corner sources obtained with CFDBF with DR for different one-third-octave frequency bands, with the respective center frequencies stated above each plot. The location of the line source is plotted as a solid black line.

$$L_p = L_{p,l} + 10 \log_{10} \left[\frac{\frac{\pi}{4}}{\arctan\left(\frac{l}{2}\right)} \right]. \quad (9)$$

where l is the length of the reduced integration area and the term $\pi/4$ comes from the solution of the arctan term in Eq. (6) for the full span ($l = 2$ m and $h = 1$ m), and consequently, $\arctan(1) = \pi/4$. For low frequencies, however, this workaround is expected to fail.

To demonstrate the added value of the ISPI method, 5 ROIs were defined. The span was divided into 3 segments. Furthermore, two ROIs were defined around the corner source locations. The width of the ROIs for all cases was $w = 0.04$ m and the mesh size was $\Delta x = 0.01$ m. The dimensions of each ROI are:

- A central ROI that goes from $z = -0.333$ m to $z = 0.333$ m, i.e., $l = 0.666$ m.
- Two lateral ROIs that go from $z = -0.990$ m to $z = -0.333$ m, and from $z = 0.333$ m to $z = 0.990$ m, i.e., $l = 0.657$ m for both ROIs.
- Two corner ROIs that at $z = -1$ m and $z = 1$ m, respectively.

Figure 8 shows the ISPI and the SPI results of the mid-span integration area. Results obtained with CLEAN-SC are included as well. All results were corrected to full span, using Eq. (9). It is observed that both SPI and CLEAN-SC fail at low frequencies, say below 700 Hz. The ISPI results, however, show very small errors (with maximum differences per frequency of 0.18 dB) for the full frequency range. The errors made by ISPI technique increase in a steady and slow manner with increasing frequency.

The average absolute errors ε made by each method are gathered in Table 3. The three methods show relatively small errors, although, for frequencies lower than 700 Hz, SPI considerably overpredicts the results and CLEAN-SC shows an oscillating behavior. The results obtained with the ISPI technique collapse almost perfectly with the exact solution.

Table 3: Average absolute errors made by each method with respect to the exact solution.

Method	ε , [dB]
SPI	1.4031
CLEAN-SC	0.9266
ISPI	0.0754

5 SENSITIVITY ANALYSIS FOR SPIL

A sensitivity analysis was performed for the SPIL method to investigate the influence of the parameters defining the ROI. Only the SPIL method is studied here for brevity reasons, but sensitivity analyses for the SPI and ISPI techniques are expected to provide similar results, and are left as future work. The ROI in Fig. 3 (shaded in orange) has four main parameters:

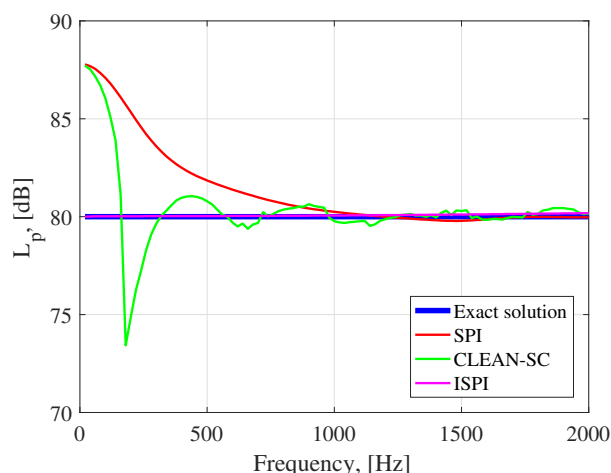


Figure 8: Results of the line-source with corner sources benchmark for the SPI, CLEAN-SC and ISPI methods with $w = 0.04$ m.

1. The width in the chordwise direction w .
2. The length in the spanwise direction l .
3. The error in the location of the simulated line source chosen by the user x_0 .
4. The spacing between grid points Δx .

For simplicity's sake, only integration lines parallel to the “experimental” line source are considered. This assumption is easily fulfilled in practical experiments, where even though the exact location of the noise source is not known *a priori*, the orientation of the model (such as an airfoil) with respect to the microphone array can be accurately determined. Moreover, all the ROIs considered here are symmetric with respect to the $z = 0$ plane and are contained in the $y = 0$ plane, i.e., the correct source distance to the array. The influence of the distance of the scan plane to the array was not investigated in this paper, but it has been previously addressed in the literature [48].

5.1 Chordwise extension

Different ROI widths w were tested (considering $x_0 = 0$, $l = 2$ m and $\Delta x = 0.01$ m) and plotted in Fig. 9a. The average absolute errors ε made for each width case are presented in Fig. 9b. Acceptable results are obtained with widths up to 0.1 m (with $\varepsilon \approx 1$ dB). After that threshold value, the error rapidly increases due to the inclusion of sidelobes in the ROI, until what looks like an asymptotic value of about 9 dB at around $w = 2$ m, which is comparable to the errors presented in Table 2 for DAMAS and orthogonal beamforming. The improvement of the results by reducing w also seems to have an asymptotic behavior. For example, reducing $w = 0.04$ m to $w = 0.02$ m only reduces ε by less than 0.01 dB. Therefore, there seems to be an acceptable range of integration widths for which the method works well.

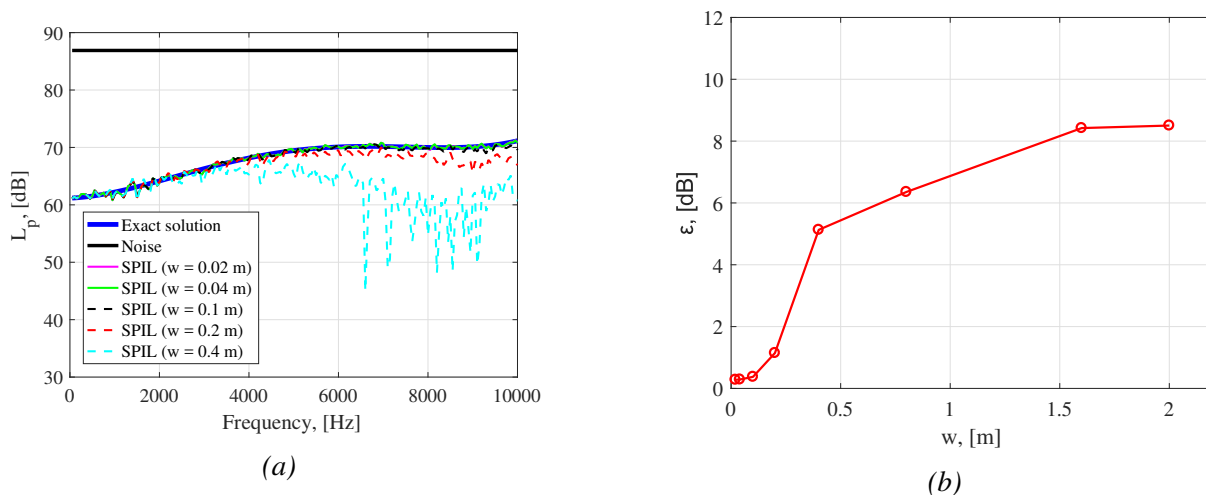


Figure 9: (a) Results of the sensitivity analysis performed for the SPIL method with respect to the ROI width w . Adapted from [19]. (b) Average absolute errors ϵ made for each width case.

5.2 Spanwise extension

As it was explained in section 4.2, L_p explicitly depends on the length of the ROI l . Therefore, a correction factor needs to be applied to the solutions obtained with ROI lengths smaller than the whole span (i.e., with $l < 2$ m), see Eq. (9). This correction was not necessary for Fig. 9, since the whole span was considered.

To investigate the influence of the choice of the ROI length, several tests were performed using different values of l (considering $x_0 = 0$, $w = 0.1$ m and $\Delta x = 0.01$ m) and the results are gathered in Fig. 10a. The average absolute errors ϵ made for each length case are presented in Fig. 10b. It seems that the error decreases when l is increased. The results for considerably short integration lengths still present relatively good results, with $\epsilon \leq 2$ dB. It seems that an increasing error occurs when reducing the value of l , especially for frequencies below 2000 Hz. The influence of the spanwise extension seems to have a lower impact in the results than the chordwise extension, see Fig. 9. Hence, the SPIL method is considered as robust with respect to the choice of the ROI length.

5.3 Error in line location

One of the unknowns when measuring trailing-edge noise in aeroacoustic experiments is the exact location of the line source. To analyze the robustness of the SPIL method with respect to this variable, several tests were performed considering different locations of the simulated line source x_0 , see Fig. 3. The length of the ROI and mesh fineness were kept constant as $l = 2$ m and $\Delta x = 0.01$ m. Two different ROI widths were tested $w = 0.04$ m and $w = 0.1$ m, and the obtained frequency spectra are presented in Fig. 11a and Fig. 11b, respectively. It can be observed that the differences with the exact solution rapidly increase after a threshold value of $x_0 = 0.02$ m with errors of about 20 dB for certain frequencies. This phenomenon is even more pronounced for the narrow width case ($w = 0.04$ m).

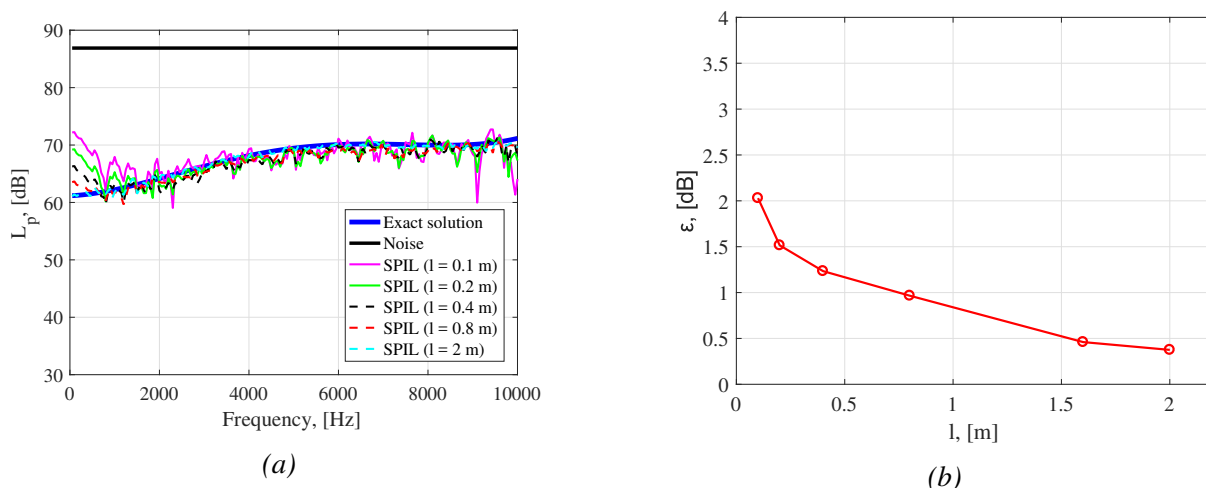


Figure 10: (a) Results of the sensitivity analysis performed for the SPIL method with respect to the ROI length l , corrected using Eq. (9). (b) Average absolute errors ϵ made for each length case.

Figure 11c depicts the values of ϵ for different values of x_0 for both cases of w . An almost-symmetric behavior with respect to $x_0 = 0$ is observed, which fits the relatively simple geometry of the benchmark. A sharp minimum of ϵ is found for $x_0 = 0$ for both cases, but the narrower width ($w = 0.04$ m) presents an even sharper minimum.

Figure 11d presents the $L_{p,\text{overall}}$ (see Eq. 8) values versus x_0 for both cases of w . A similar behavior as in Fig. 11c is observed, with the difference that, in this case, a maximum is observed for $x_0 = 0$, instead of a minimum. Once again, the narrower ROI shows a sharper peak, with still an almost-symmetric behavior with respect to $x_0 = 0$. This is an important finding in order to search for the correct location of a line source in practical cases. A fast sweep can be performed for different x_0 values using small values of w and select the x_0 value that provides a maximum for $L_{p,\text{overall}}$. In practice, the expected range of x_0 is typically in the order of centimeters, so the computational demand of this procedure is not high.

5.4 Mesh fineness

Tests were performed using several spacings between grid points Δx (considering $x_0 = 0$, $w = 0.04$ m and $l = 2$ m) and plotted in Fig. 12a. The average absolute errors ϵ made for each width case are presented in Fig. 12b. The mesh fineness does not seem to influence the results in a strong manner. Only very coarse grids ($\Delta x = 0.5$ m, i.e., only 5 grid points in the z direction) seem to diverge from the exact solution, especially after 9 kHz. In practice, there is normally no need for using such coarse grids. Grids with $\Delta x \leq 0.2$ show values of ϵ lower than 1 dB, which is considered as acceptable. The improvement of the results by reducing Δx seems to have an asymptotic behavior once again. For example, reducing $\Delta x = 0.01$ m to $\Delta x = 0.001$ m only reduces ϵ by around 0.003 dB, but increases the computational time by 100 times. Hence, the SPIL method seems to be quite robust with respect to the choice of the mesh fineness and offers acceptable results for relatively coarse grids.

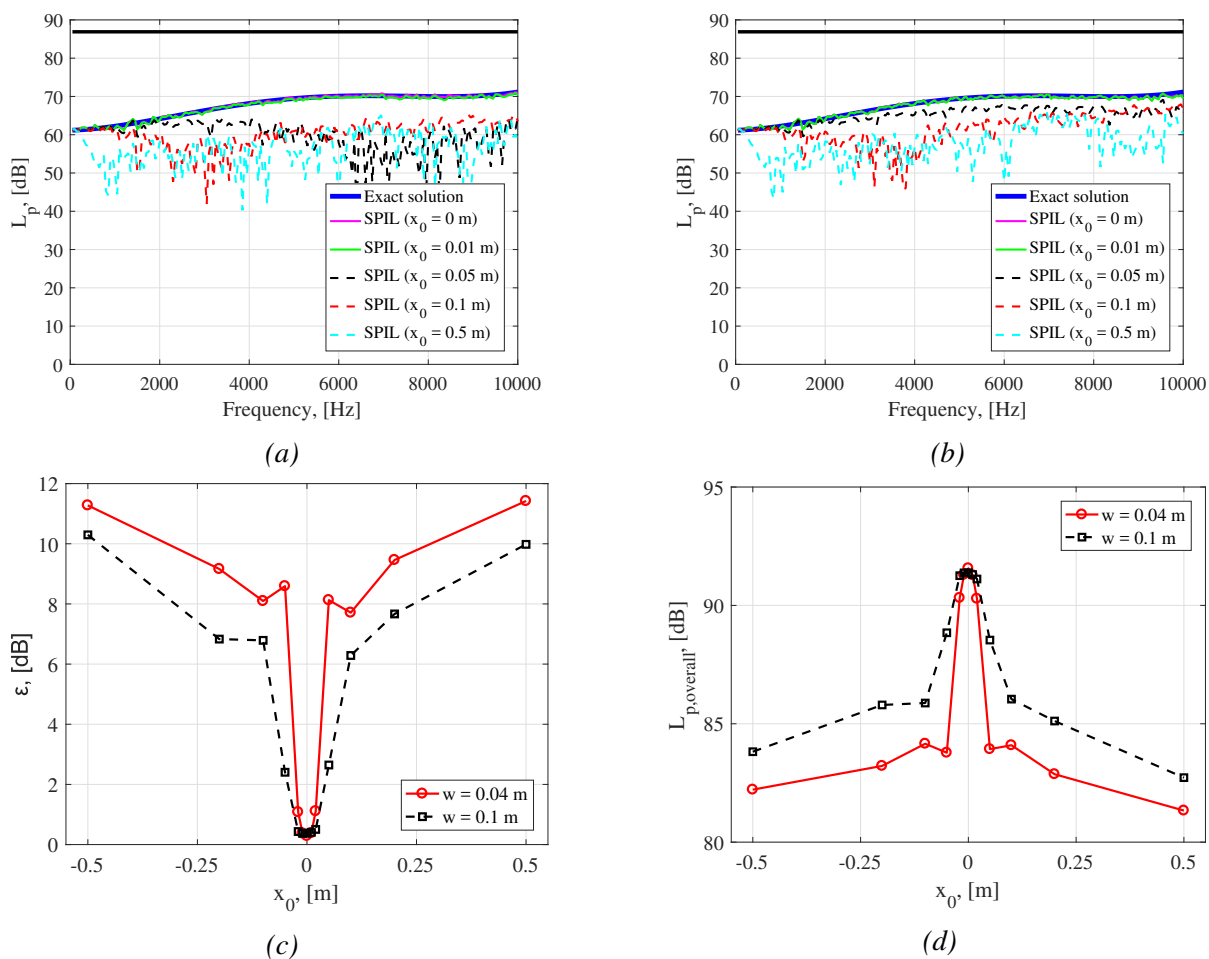


Figure 11: Results of the sensitivity analysis performed for the SPIL method with respect to the error in the line location x_0 for (a) $w = 0.04$ m and (b) $w = 0.1$ m. (c) Average absolute errors ϵ and (d) $L_{p,overall}$ for each x_0 case.

6 CONCLUSIONS

In this paper, three integration methods intended to accurately solve distributed sound sources, such as trailing-edge noise are introduced. The first technique (SPI) is based on a single monopole source, the second one (SPIL) considers the presence of a single line source, whereas the last one (ISPI) extends the assumption to several line sources.

Explanations about how the methods work are provided and the performance of each method is evaluated in two simulated benchmark cases and compared to other well-known acoustic imaging techniques. Both benchmark cases represent examples of practical wind-tunnel measurements of trailing-edge noise. SPIL showed the best results for the first benchmark case with respect to other methods, such as DAMAS, CLEAN-SC or functional beamforming. ISPI outperformed SPI and CLEAN-SC, allowing for the exclusion of unwanted noise sources, such as corner sources, which are usually present in the junction between the airfoil and the wind-tunnel walls. The computational demand for the three techniques is considerably low since they

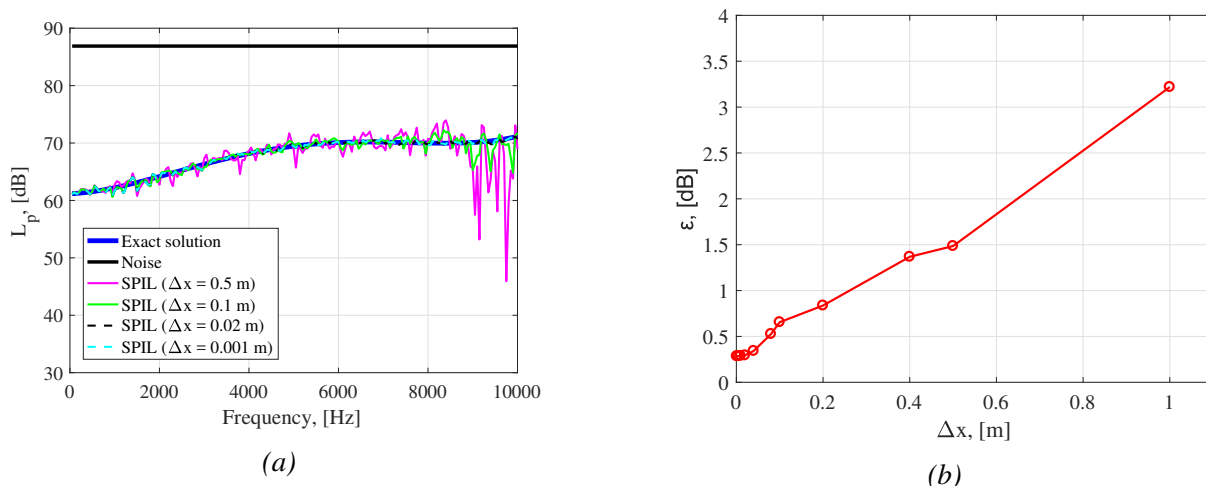


Figure 12: (a) Results of the sensitivity analysis performed for the SPIL method with respect to the spacing between grid points Δx . (b) Average absolute errors ϵ made for each width case.

are based on the CFDBF algorithm.

A sensitivity analysis for the SPIL method showed that it is considerably robust to the choice of the integration area, in both shape and position. The fineness of the grid does not seem to influence the results within a sensible range. Recommendations are provided for practical experiments, such as how to approximate the exact location of the line source.

All in all, the use of the SPIL technique is recommended for the study of distributed sound sources with little variation in the sound level and, in case the presence of unwanted noise sources, such as corner sources, is expected, ISPI is the preferred method.

References

- [1] D. H. Johnson and D. E. Dudgeon, *Array Signal Processing, Concepts and Techniques* (P T R Prentice Hall, Englewood Cliffs, 1993) ISBN: 9780130485137.
- [2] T. Mueller, *Aeroacoustic Measurements* (Springer Science & Business Media, 2002) p. 313, ISBN-978-3-642-07514-8.
- [3] R. Merino-Martínez, P. Sijtsma, M. Snellen, T. Ahlefeldt, J. Antoni, C. Bahr, D. Blacodon, D. Ernst, A. Finez, S. Funke, T. Geyer, S. Haxter, G. Herold, X. Huang, W. Humphreys, Q. Leclère, A. Malgoezar, U. Michel, T. Padois, A. Pereira, C. Picard, E. Sarradj, H. Siller, D. G. Simons, and C. Spehr, *Aircraft Noise Generation and Assessment: A review of acoustic imaging methods using phased microphone arrays*, *CEAS aeroacoustic journal*, *CEAS Aeronautical journal* (2017), under review process.
- [4] P. Sijtsma and R. Stoker, *Determination of Absolute Contributions of Aircraft Noise Components Using Fly-over Array Measurements*, in *10th AIAA/CEAS Aeroacoustics Conference, May 10 – 12 2004, Manchester, United Kingdom* (2004) AIAA paper 2004-2958.

- [5] P. Sijtsma, *Acoustic beamforming for the ranking of aircraft noise*, Tech. Rep. NLR-TP-2012-137 (National Aerospace Laboratory (NLR), Anthony Fokkerweg 2, 1059 CM Amsterdam, P.O. Box 90502, 1006 BM Amsterdam, The Netherlands, 2012).
- [6] M. Snellen, R. Merino-Martinez, and D. G. Simons, *Assessment of aircraft noise sources variability using an acoustic camera*, in *5th CEAS Air & Space Conference. Challenges in European Aerospace. September 7 – 11 2015, Delft, Netherlands* (2015).
- [7] R. Merino-Martinez, M. Snellen, and D. G. Simons, *Determination of Aircraft Noise Variability Using an Acoustic Camera*, in *23rd International Congress on Sound and Vibration, July 10 – 14 2016, Athens, Greece* (2016).
- [8] M. Snellen, R. Merino-Martinez, and D. G. Simons, *Assessment of noise level variability on landing aircraft using a phased microphone array*, *Journal of Aircraft* **54**, 2173 (2017).
- [9] S. Oerlemans and P. Sijtsma, *Acoustic Array Measurements of a 1:10.6 Scaled Airbus A340 Model*, in *10th AIAA/CEAS Aeroacoustics Conference, May 10 – 12, 2004, Manchester, United Kingdom* (2004) AIAA paper 2004-2924.
- [10] P. Sijtsma, *Phased array beamforming applied to wind tunnel and fly-over tests*, Tech. Rep. NLR-TP-2010-549 (National Aerospace Laboratory (NLR), Anthony Fokkerweg 2, 1059 CM Amsterdam, P.O. Box 90502, 1006 BM Amsterdam, The Netherlands, 2010).
- [11] C. Arce León, R. Merino-Martinez, D. Ragni, F. Avallone, and M. Snellen, *Boundary layer characterization and acoustic measurements of flow-aligned trailing edge serrations*, *Experiments in Fluids* **57**, 22 (2016).
- [12] C. Arce León, R. Merino-Martinez, D. Ragni, F. Avallone, F. Scarano, S. Pröbsting, M. Snellen, D. G. Simons, and J. Madsen, *Effect of trailing edge serration-flow misalignment on airfoil noise emission*, *Journal of Sound and Vibration* **405**, 19 (2017).
- [13] C. Arce León, R. Merino-Martinez, S. Pröbsting, D. Ragni, and F. Avallone, *Acoustic Emissions of Semi-Permeable Trailing Edge Serrations*, *Acoustics Australia* **1** (2017), 10.1007/s40857-017-0093-8.
- [14] C. Arce León, R. Merino-Martinez, D. Ragni, S. Pröbsting, F. Avallone, A. Singh, and J. Madsen, *Trailing Edge Serrations – Effect of Their Flap Angle on Flow and Acoustics*, in *7th International Meeting on Wind Turbine Noise, May 2 – 5 2017, Rotterdam, the Netherlands* (2017).
- [15] R. Merino-Martinez, W. C. P. van der Velden, F. Avallone, and D. Ragni, *Acoustic measurements of a DU96-W-180 airfoil with flow-misaligned serrations at a high Reynolds number in a closed-section wind tunnel*, in *7th International Meeting on Wind Turbine Noise, May 2 – 5 2017, Rotterdam, the Netherlands* (2017).
- [16] F. Avallone, W. C. P. van der Velden, R. Merino-Martinez, and D. Ragni, *Near-wall pressure fluctuations over noise reduction add-ons*, in *23rd AIAA/CEAS Aeroacoustics Conference. June 5 – 9 2017. Denver, CO, USA* (2017) AIAA paper 2017-4171.

- [17] A. Rubio Carpio, R. Merino-Martinez, F. Avallone, D. Ragni, M. Snellen, and S. van der Zwaag, *Broadband Trailing Edge Noise Reduction Using Permeable Metal Foams*, in *46th International Congress and Exposition of Noise Control Engineering*, 27–30 August, 2017, Hong Kong (2017).
- [18] T. F. Brooks and W. M. Humphreys, *Effect of Directional Array Size on the Measurement of Airframe Noise Components*, in *5th AIAA/CEAS Aeroacoustics Conference*. Bellevue, WA, USA (1999) AIAA paper 1999–1958.
- [19] E. Sarradj, G. Herold, P. Sijtsma, R. Merino-Martinez, A. M. N. Malgoezar, M. Snellen, T. F. Geyer, C. J. Bahr, R. Porteous, D. J. Moreau, and C. J. Doolan, *A microphone array method benchmarking exercise using synthesized input data*, in *23rd AIAA/CEAS Aeroacoustics Conference*. June 5 – 9 2017. Denver, CO, USA (2017) AIAA paper 2017–3719.
- [20] C. J. Bahr, T. F. Brooks, L. Brusniak, R. P. Dougherty, W. M. Humphreys, R. Schröder, and J. R. Underbrink, *Array Analysis Methods Benchmarking – Initial Planning Meeting*, in *20th AIAA/CEAS Aeroacoustics Conference*, June 16 – 20 2014, Atlanta, GA, USA (2014) array Analysis Methods Meeting.
- [21] C. J. Bahr, *Phased Array Methods Panel Session: Introduction, Moving Forward, and Discussion*, in *21st AIAA/CEAS Aeroacoustics Conference*, June 22 – 26 2015, Dallas, TX, USA (2015) array Analysis Methods Meeting.
- [22] C. J. Bahr, *Phased Array Methods Panel Session: Introduction, Year 2 Progress, and Discussion*, in *6th Berlin Beamforming Conference*, February 29 – March 1 2016, Berlin, Germany (2016).
- [23] C. J. Bahr, *Phased Array Methods Panel Session: Introduction, Year 2 Summary, and Discussion*, in *22nd AIAA/CEAS Aeroacoustics Conference*. May 30 – June 1 2016. Lyon, France (2016) array Methods Panel Session.
- [24] P. Sijtsma, *CLEAN based on spatial source coherence*, *International Journal of Aeroacoustics* **6**, 357 (2007), SAGE Publications Ltd. London, United Kingdom.
- [25] P. Sijtsma, R. Merino-Martinez, A. M. N. Malgoezar, and M. Snellen, *High-Resolution CLEAN-SC: Theory and Experimental Validation*, *International Journal of Aeroacoustics* **16**, 274 (2017), SAGE Publications Ltd. London, United Kingdom.
- [26] P. Sijtsma, R. Merino-Martinez, A. M. N. Malgoezar, and M. Snellen, *High-Resolution CLEAN-SC: Theory and Experimental Validation*, in *23rd AIAA/CEAS Aeroacoustics Conference*. June 5 – 9 2017. Denver, Colorado, USA (2017) AIAA paper 2017–3841.
- [27] T. F. Brooks and W. M. Humphreys, *A Deconvolution Approach for the Mapping of Acoustic Sources (DAMAS) determined from phased microphone arrays*, in *10th AIAA/CEAS Aeroacoustics Conference*. May 10 – 12 2004. Manchester, UK (2004) AIAA paper 2004–2954.

- [28] R. P. Dougherty, *Functional Beamforming*, in *5th Berlin Beamforming Conference, February 19 – 20 2014, Berlin, Germany* (GFaI, e.V., Berlin, 2014).
- [29] R. P. Dougherty, *Functional Beamforming for Aeroacoustic Source Distributions*, in *20th AIAA/CEAS Aeroacoustics Conference. June 16 – 20 2014. Atlanta GA, USA* (2014) AIAA paper 2014–3066.
- [30] R. Merino-Martinez, M. Snellen, and D. G. Simons, *Functional beamforming applied to imaging of flyover noise on landing aircraft*, *Journal of Aircraft* **53**, 1830 (2016).
- [31] R. Merino-Martinez, M. Snellen, and D. G. Simons, *Functional Beamforming Applied to Full Scale Landing Aircraft*, in *6th Berlin Beamforming Conference, February 29 – March 1 2016, Berlin, Germany* (GFaI, e.V., Berlin, 2016) BeBeC–2016–D12.
- [32] T. Yardibi, J. Li, P. Stoica, N. S. Zawodny, and L. N. Cattafesta III, *A covariance fitting approach for correlated acoustic source mapping*, *Journal of the Acoustical Society of America* **127**, 2920 (2010).
- [33] E. Sarradj, C. Schulze, and A. Zeibig, *Identification of Noise Source Mechanisms using Orthogonal Beamforming*, in *Noise and Vibration: Emerging Methods* (2005).
- [34] E. Sarradj and C. Schulze, *Practical Application of Orthogonal Beamforming*, in *Proceedings Euronoise 2006* (2006).
- [35] E. Sarradj, *A fast signal subspace approach for the determination of absolute levels from phased microphone array measurements*, *Journal of Sound and Vibration* **329**, 1553 (2010).
- [36] S. Oerlemans, *Detection of aeroacoustic sound sources on aircraft and wind turbines*, Phd thesis, University of Twente, Enschede (2009).
- [37] D. Ernst, C. Spehr, and T. Berkefeld, *Decorrelation of acoustic wave propagation through the shear layer in open jet wind tunnel*, in *21st AIAA/CEAS Aeroacoustics Conference, June 22 – 26 2015, Dallas, TX, USA* (2015) AIAA paper 2015–2976.
- [38] R. Merino-Martinez, L. Bertsch, M. Snellen, and D. G. Simons, *Analysis of landing gear noise during approach*, in *22nd AIAA/CEAS Aeroacoustics Conference. May 30 – June 1 2016. Lyon, France* (2016) AIAA paper 2016–2769.
- [39] R. Merino-Martinez, E. Neri, M. Snellen, J. Kennedy, D. Simons, and G. Bennett, *Comparing flyover noise measurements to full-scale nose landing gear wind-tunnel experiments for regional aircraft*, in *23rd AIAA/CEAS Aeroacoustics Conference. June 5 – 9 2017. Denver, Colorado, USA* (2017) AIAA paper 2017–3006.
- [40] C. L. Lawson and R. J. Hanson, *Solving least squares problems*, edited by S. for Industrial and A. Mathematics (Englewood Cliffs, New Jersey, 1974) ISBN 0–89871–356–0.
- [41] M. Tuinstra and P. Sijtsma, *Suppression of spurious noise sources in airfoil self-noise measurements*, in *21st AIAA/CEAS Aeroacoustics Conference. June 22 – 26 2015. Dallas, TX, USA* (2015) AIAA paper 2015–2689.

- [42] C. C. J. Pagani, D. S. Souza, and M. A. F. Medeiros, *Slat Noise: Aeroacoustic Beamforming in Closed-Section Wind Tunnel with Numerical Comparison*, *AIAA Journal* **54**, 2100 (2016).
- [43] P. Sijtsma, *Analytical Benchmark 1*, in 22nd AIAA/CEAS Aeroacoustics Conference. May 30 – June 1 2016. Lyon, France (2016) Presentation in Microphone Array Methods Discussion Panel.
- [44] K. Ehrenfried and L. Koop, *A comparison of iterative deconvolution algorithms for the mapping of acoustic sources*, in 12th AIAA/CEAS Aeroacoustics Conference. May 8 – 10 2006. Cambridge, Massachusetts, USA (2006) AIAA paper 2006–2711.
- [45] G. Herold, T. F. Geyer, and E. Sarradj, *Comparison of Inverse Deconvolution Algorithms for High-Resolution Aeroacoustic Source Characterization*, in 23rd AIAA/CEAS Aeroacoustics Conference. June 5 – 9 2017. Denver, Colorado, USA (2017) AIAA paper 2017–4177.
- [46] R. P. Dougherty, *Cross Spectral Matrix Diagonal Optimization*, in 6th Berlin Beamforming Conference, February 29 – March 1, 2016, Berlin, Germany (GFaI, e.V., Berlin, 2016).
- [47] J. Hald, *Removal of incoherent noise from an averaged cross-spectral matrix*, *Journal of the Acoustical Society of America* **142**, 846 (2017).
- [48] E. Sarradj, *Three-Dimensional Acoustic Source Mapping with Different Beamforming Steering Vector Formulations*, *Advances in Acoustics and Vibration* **2012**, 1 (2012).